



Alpha Particle Temperature Anisotropy in Earth's Magnetosheath

Haley DeWeese¹ , Bennett A. Maruca^{1,2} , Ramiz A. Qudsi³ , Alexandros Chasapis⁴ , Mark Pultrone⁵, Elliot Johnson¹ , Sarah K. Vines⁶ , Michael A. Shay^{1,2} , William H. Matthaeus^{1,2} , Roman G. Gomez⁷ , Stephen A. Fuselier^{7,8} , Barbara L. Giles⁹ , Daniel J. Gershman⁹ , Christopher T. Russell¹⁰ , Robert J. Strangeway¹⁰ , James L. Burch⁷ , and Roy B. Torbert⁷

¹ Department of Physics & Astronomy, University of Delaware, Newark, DE, USA

² Bartol Research Institute, Newark, DE, USA

³ Center for Space Physics, Boston University, Boston, MA, USA

⁴ Laboratory for Atmospheric and Space Physics, University of Colorado Boulder, Boulder, CO, USA

⁵ Lockheed Martin, Moorestown, NJ, USA

⁶ The Johns Hopkins Applied Physics Laboratory, Laurel, MD, USA

⁷ Southwest Research Institute, San Antonio, TX, USA

⁸ University of Texas at San Antonio, San Antonio, TX, USA

⁹ NASA Goddard Space Flight Center, Greenbelt, MD, USA

¹⁰ Department of Earth, Planetary and Space Sciences, University of California Los Angeles, Los Angeles, CA, USA

Received 2022 July 14; revised 2022 September 28; accepted 2022 October 3; published 2022 December 7

Abstract

In magnetized plasmas, temperature anisotropy manifests as distinct temperatures ($T_{\perp j}$, $T_{\parallel j}$). Numerous prior studies have demonstrated that as plasma beta ($\beta_{\parallel j}$) increases, the range of temperature anisotropy ($R_j = T_{\perp j}/T_{\parallel j}$) narrows. This limiting effect is conventionally taken as evidence that kinetic microinstabilities are active in the plasma, and has been previously observed for protons in the magnetosheath. This study is the first to use data from the Magnetic Multiscale Mission to investigate these instability-driven limits on alpha particle (ionized helium) anisotropy in Earth's magnetosheath. The distribution of data over the ($\beta_{\parallel j}$, R_j) plane was plotted and shows the characteristic narrowing in the range of R_j -values as $\beta_{\parallel j}$ increases. The contours of the data distribution align well with the contours of the constant growth rate for the ion cyclotron, mirror, parallel firehose, and oblique firehose instabilities, which were calculated using linear Vlasov theory.

Unified Astronomy Thesaurus concepts: Space plasmas (1544); Solar wind (1534); Planetary magnetospheres (997)

1. Introduction

The solar wind is the stream of magnetized plasma that flows out supersonically from the Sun's corona. As it travels outwards, some solar wind plasma will inevitably encounter the magnetic fields of the planets orbiting the Sun. The plasma flow goes from supersonic to subsonic as it crosses a planet's bow shock, which creates regions of space plasma around the planet that have different physical properties than the solar wind, such as the layers of Earth's magnetosphere. One trait these regions of space plasma have in common is that they are rarely observed to be in thermal equilibrium, owing to their high temperatures and low particle density.

Any deviation away from a Maxwellian velocity distribution function (VDF) represents a source of free energy, and if the plasma departs enough from equilibrium and gains enough free energy, kinetic microinstabilities can develop. These instabilities generate waves that create enhanced fluctuations in the magnetic field that act to pitch-angle scatter the particles, driving the plasma closer to equilibrium (Gary et al. 1993, 1997; Bale et al. 2009).

Kinetic microinstabilities can be driven by a number of different nonequilibrium properties. Though space plasma ions have been observed to exhibit various non-LTE features including beams, unequal temperatures, and relative drift

(Marsch 2006; Bourouaine et al. 2013; Verscharen et al. 2019)—this study focuses specifically on temperature anisotropy.

Temperature anisotropy in space plasmas develops because the transport of energy in the plasma is direction dependent, giving rise to distinct parallel (T_{\parallel}) and perpendicular (T_{\perp}) temperatures with respect to the background magnetic field B_0 (Maruca et al. 2018). Often when discussing temperature anisotropy, it is useful to introduce the ratio:

$$R_j = \frac{T_{\perp j}}{T_{\parallel j}} \quad (1)$$

where $T_{\perp j}$ and $T_{\parallel j}$ are the perpendicular and parallel temperatures for a given particle species j respectively. A value of $R_j = 1$ would correspond to temperature isotropy, where both the parallel and perpendicular temperatures are equal.

Numerous prior studies (see Section 2) have examined how kinetic microinstabilities affect temperature anisotropies for various ions in different space plasma regions. This study considers plasma from Earth's magnetosheath, the region of subsonic solar wind plasma enveloping the magnetosphere. It is the first to look into how kinetic microinstabilities in the magnetosheath limit alpha particle temperature anisotropies, using data from the Magnetic Multiscale (MMS) Mission. Section 2 provides an overview of the theory of temperature anisotropy and associated instabilities. Section 3 describes the specific MMS observations used in this study, while Section 4



Original content from this work may be used under the terms of the [Creative Commons Attribution 4.0 licence](https://creativecommons.org/licenses/by/4.0/). Any further distribution of this work must maintain attribution to the author(s) and the title of the work, journal citation and DOI.

Table 1
Instabilities Driven by Ion Temperature Anisotropies

Triggering Mechanism	Parallel Instabilities ($\mathbf{k} \parallel \mathbf{B}_0$)	Oblique Instabilities ($\mathbf{k} \nparallel \mathbf{B}_0$)
$T_{\perp j} > T_{\parallel j}$	Ion Cyclotron	Mirror
$T_{\perp j} < T_{\parallel j}$	Parallel Firehose	Oblique Firehose

details how they were analyzed. Section 5 discusses the results of this analysis.

2. Background

The presence of non-LTE features, including temperature anisotropy, in a plasma can provide the free energy for small-amplitude fluctuations to grow exponentially. Such a growing mode constitutes a *kinetic microinstability*.

In linear Vlasov theory, a uniform, static plasma state is perturbed by a small-amplitude fluctuation of wavevector \mathbf{k} and angular frequency ω . By expanding Maxwell’s equations and the Vlasov equation to first order in this perturbation (see, e.g., Gary 2005), a dispersion relation can be derived and used to find the value of ω for any given \mathbf{k} value. Each ω will also have a real and imaginary component, the latter of which is also called the growth rate γ . If $\gamma \leq 0$, the fluctuation is either constant or damped with a decaying amplitude and is considered a wave. Alternatively, if $\gamma > 0$ then the fluctuation has an exponentially growing amplitude and is considered an instability.

If the temperature becomes sufficiently anisotropic (i.e., R_j departs far enough from unity for some particle species j), one or more microinstabilities may develop. Linear Vlasov theory predicts four instabilities driven by ion temperature anisotropy in a collisionless, magnetized plasma with bi-Maxwellian VDFs. When $T_{\perp j} > T_{\parallel j}$, the ion cyclotron and/or mirror instabilities can develop. The former has \mathbf{k} parallel to \mathbf{B}_0 while the other has it at an oblique angle. Conversely, $T_{\perp j} < T_{\parallel j}$ may drive the parallel and/or oblique firehose instabilities, which (as their names suggest), are modes with \mathbf{k} parallel and oblique to \mathbf{B}_0 , respectively. Table 1 summarizes the basic properties of these four instabilities.

The overall growth rate, γ_{\max} of any one of the instabilities listed in Table 1 is defined as the maximum γ -value over all \mathbf{k} -values associated with that instability. The value of γ_{\max} is never negative since $\gamma = 0$ for the degenerate $\mathbf{k} = 0$ mode. Thus, when $\gamma_{\max} = 0$, the instability is regarded as inactive since there are no growing modes. A positive γ_{\max} -value indicates instability, though plasma for which γ_{\max} is “small” (e.g., $< 10^{-3}\Omega_p$) is often termed “marginally unstable” since plasma conditions might change prior to the unstable modes growing enough to become nonlinear and begin scattering particles in phase space.

The value of γ_{\max} for any given instability depends on the plasma conditions, most notably on R_j . In the absence of temperature anisotropy ($R_j = 1$), the plasma is stable ($\gamma_{\max} = 0$) since the plasma is already in LTE. Nevertheless, a departure from isotropy ($R_j \neq 1$) does not automatically drive an instability. Indeed, if R_j is varied while the other plasma parameters are kept fixed, there is a range of R_j -values for which $\gamma_{\max} = 0$.

Aside from R_j , the growth rate (γ_{\max}) of ion temperature anisotropy instabilities (Table 1) is most affected by plasma

beta:

$$\beta_{\parallel j} = \frac{n_j k_B T_{\parallel j}}{B^2 / (2\mu_0)} \quad (2)$$

where n_j is the particle species density, k_B is the Boltzmann constant, and μ_0 is the vacuum permeability. As $\beta_{\parallel j}$ increases, the range of R_j -values for which the plasma is stable (i.e., $\gamma_{\max} = 0$) narrows. Low- $\beta_{\parallel j}$ plasmas can exhibit significant anisotropies while remaining stable, but instabilities will develop in high- $\beta_{\parallel j}$ plasma with even modest anisotropies.

Numerous statistical studies of protons in space plasmas have found that the distribution of ($\beta_{\parallel p}$, R_p)-values aligns well with γ_{\max} -contours computed with linear Vlasov theory. Most of these studies have considered the solar wind both near Earth (Gary et al. 2001; Kasper et al. 2002, 2003; Hellinger et al. 2006; Bale et al. 2009; Maruca et al. 2011; Osman et al. 2012; Jansen et al. 2018; Zhang et al. 2018) and at other distances from the Sun (Marsch et al. 2004; Matteini et al. 2007; Huang et al. 2020; Lentz et al. 2021). Similar observational evidence for the action of proton temperature anisotropy instabilities has also been found in Earth’s magnetosheath (Anderson et al. 1994; Phan et al. 1994; Gary et al. 1997; Tan et al. 1998) and magnetosphere (Gary et al. 1995; Anderson et al. 1996). Most recently, the ($\beta_{\parallel p}$, R_p) relationship has been identified in Jupiter’s magnetosheath (Bandyopadhyay et al. 2022). Taken collectively, these studies strongly suggest that kinetic microinstabilities provide ubiquitous constraints on proton temperature anisotropy across space plasmas.

In comparison, instability limits on alpha particle temperature anisotropy have received less attention. Maruca et al. (2012) and Bourouaine et al. (2013) found that the distribution of solar wind observations of ($\beta_{\parallel \alpha}$, R_{α})-value aligned well with γ_{\max} contours computed from linear Vlasov theory. Chen et al. (2016) also considered the effects of alpha particle temperature anisotropy but primarily in the context of fluid instabilities rather than kinetic microinstabilities.

3. Observations

3.1. Instrumentation

MMS (Burch et al. 2016), launched in 2015, is comprised of a constellation of four spacecraft. All of the spacecraft are identically instrumented and are fitted with instruments designed to measure plasma in Earth’s magnetosphere.

For this study, proton and alpha particle moments were taken from the Hot Plasma Composition Analyzer (HPCA; Young et al. 2016). This instrument is composed of an electrostatic analyzer and a time-of-flight analyzer, which allows it to return velocity distributions for four different ion species (H^+ , He^+ , He^{++} , and O^+)¹¹ in the energy range from 1 eV to 40 keV.

The magnetic field data were obtained using measurements from the Flux Gate Magnetometers (Russell et al. 2016), which are a part of the FIELDS instrumentation suite, and provides measurements of \mathbf{B} at a cadence of 128 Hz (Torbert et al. 2016).

¹¹ He^+ and O^+ do not occur with sufficient abundance in the magnetosheath and were thus disregarded for this study.

Table 2
Periods of MMS Survey-mode Data Used in This Study

Date		Time Period	
2017 Nov	14	01:48:50	02:23:05
	14	14:48:18	19:57:03
	16	12:40:43	19:12:45
	17	10:12:31	12:21:44
	19	12:15:27	16:21:26
	20	05:40:22	07:05:00
	22	05:39:45	11:08:00
	23	02:13:43	06:18:40
	25	01:26:21	07:03:05
	25	21:43:10	23:39:30
	28	01:01:40	03:10:07
	28	16:44:30	18:00:31
	30	16:22:38	22:58:05
2017 Dec	1	11:34:55	13:54:52
	3	10:28:20	17:26:20
	4	06:13:17	08:21:40
	6	08:49:25	14:02:00
	7	03:15:55	05:50:50
	9	02:59:32	08:22:30
	9 ^a	23:07:12	00:38:39
	12	03:33:23	07:20:25
	12	17:21:30	19:42:02
	14 ^a	22:12:22	02:15:32
	15	13:08:15	16:50:05
	17	19:19:43	22:47:32
	18	08:08:19	11:51:37
	20	14:19:02	16:35:02
	21	05:01:49	10:01:48
	23	10:44:48	13:45:46
	23 ^a	23:59:36	02:31:18
	26	04:04:35	08:31:22
	26	19:15:50	21:50:25
	28 ^a	22:12:05	04:02:13
	29	15:45:50	17:16:04
	31 ^b	22:09:38	
2018 Jan	1 ^b		02:11:34
	1	11:10:48	12:54:50
	3	17:55:01	19:58:44
	4	07:00:23	09:59:37
	6	13:21:47	15:24:43
	7	02:54:22	05:16:04
	9	08:50:20	11:06:07
	9 ^a	22:42:00	00:54:50
	12	03:22:50	07:02:15
	12	17:45:25	20:04:30
	15	01:11:45	02:12:44
	15	14:02:47	16:25:30
	17	18:24:44	21:59:22
	18	09:31:00	11:50:27
	20	16:34:50	18:57:15
	21	04:40:50	06:44:01
	23	09:45:10	13:05:42
	24	02:09:40	03:51:37
	26	08:02:30	10:18:10
	26	20:57:20	22:25:50
	29	04:15:00	05:08:00
	29	15:21:50	18:14:11
	31 ^c	23:29:52	
2018 Feb	1 ^c		01:11:10
	1	12:18:20	14:18:30
	3	19:30:32	21:30:30
	4	07:23:30	09:07:20
	6	13:34:00	15:47:28

Table 2
(Continued)

Date		Time Period	
2018 Feb	7	03:33:33	06:50:15
	9	09:19:20	11:34:20
	9 ^a	22:21:53	01:00:40
	12	06:15:03	07:57:15
	12	17:51:45	20:01:45
	14 ^a	23:48:44	02:40:02
	15	12:50:30	14:41:12
	17	21:38:43	23:19:02
	18	11:24:00	13:21:45
	20	14:40:45	16:34:00
	21	06:08:35	09:42:58
	23	12:12:54	13:58:45
	24	00:28:40	06:11:15
	26	07:14:10	10:06:52
	26	22:03:08	23:37:48
2018 Mar	1	01:44:30	05:12:15
	1	17:41:07	21:32:09
	4	00:43:44	02:04:00
	4	13:57:45	16:18:25
	6	17:08:58	20:04:10
	7	10:06:20	14:18:05
	9	11:06:10	14:56:40
	10	02:42:00	10:12:00
	12	07:47:23	10:29:30
	13	01:34:08	04:52:01

Notes.

^a Interval ends on the following day.

^b This is one period lasting from 2017 December 31 22:09:38 to 2018 January 1 02:11:34.

^c This is one period lasting from 2018 January 31 23:29:52 to 2018 February 1 01:11:10.

3.2. Data Selection

The data set used for this study consists of survey-mode data from one of the four spacecraft (MMS1) using specific periods within the date range of 2017 November–2018 March. The orbit of MMS passes through the solar wind, magnetosheath, and solar wind, so these time periods, which can be found in Table 2, were manually selected to only include times when the spacecraft was in the magnetosheath. Across all of these intervals, only measurements for which the proton and alpha particle measurements were valid were selected, resulting in a data set containing $N = 129,934$ measurements of proton and alpha particle moments.

4. Analysis

Figure 1 depicts four plots of T_{\parallel} versus T_{\perp} for both protons (shown in blue) and alpha particles (shown in red). To generate both proton plots, the $(T_{\parallel}, T_{\perp})$ plane was divided into a grid of bins: 100 $T_{\parallel p}$ bins by 100 $T_{\perp p}$ bins, both logarithmically spaced from $10^{1.5}$ to 10^4 K. The color of each bin indicates (on a logarithmic scale) n , the number of observations from the data set that it contains. Bins with less than 10 observations (i.e., $n = 10$) were deemed statistically insignificant and not rendered.

The top row of Figure 1 shows two joint distributions of $(T_{\perp j}, T_{\parallel j})$ -values: one for protons ($j = p$) and the other for alpha particles ($j = \alpha$). They were created using values of T_{\parallel} and T_{\perp} given in the MMS/HPCA data files, which were computed

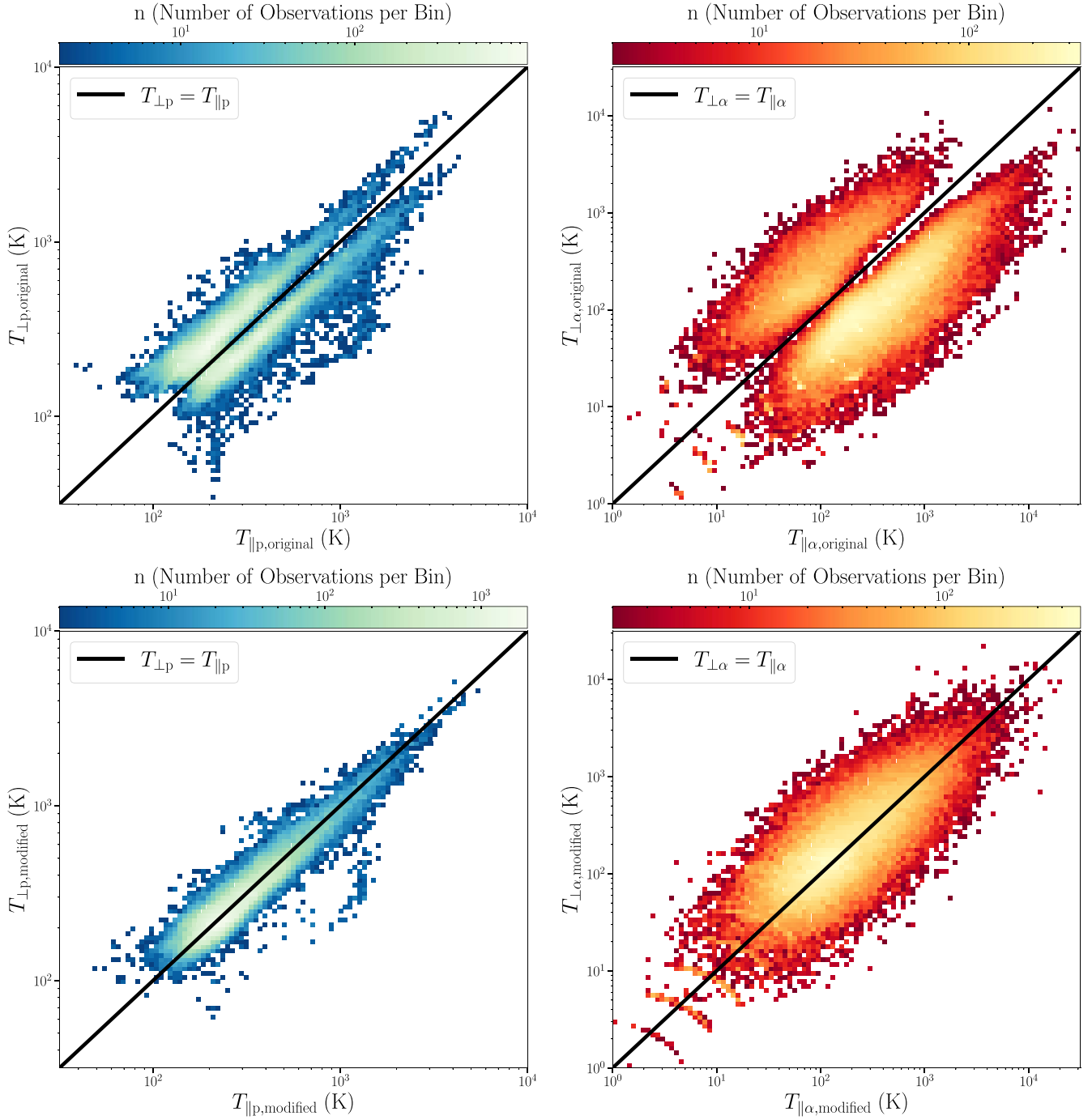


Figure 1. Four plots of the distribution of $(T_{\parallel j}, T_{\perp j})$ -values of both ions for the MMS data set specified in Table 2. Plots for protons are on the left side (colored blue) and plots for alpha particles are on the right side (colored red).

from the diagonalization of the temperature tensor (Gomez 2016). For both particle species, anisotropic plasma with either $(T_{\perp j} > T_{\parallel j})$ or $(T_{\perp j} < T_{\parallel j})$ is quite common. However, isotropic plasma that has $(T_{\perp j} \approx T_{\parallel j})$ is exceptionally rare. This unusual distribution arises not from actual observation but is instead an artifact of the diagonalization method of computing temperature components.

4.1. Temperature Transformations

Subtle complications arise when calculating the perpendicular and parallel temperature components, $T_{\perp j}$ and $T_{\parallel j}$, from a

set of particle moments as they involve both particle and magnetic field parameters. The moments of temperature tensor provided in the publicly available MMS/HPCA data files (Section 3) are given in DBCS coordinates, which may be treated as near-GSE due to the fact the positive spin axis is $\sim 3^\circ$ away from the ecliptic and will be referred to as such from here on out. (Hsu & McCarthy 2014) While the temperature tensor is in near-GSE coordinates, the magnetic field direction (the “parallel” direction) is arbitrarily oriented to the axes in this coordinate system.

One approach to computing $T_{\perp j}$ and $T_{\parallel j}$ is to diagonalize the temperature tensor. Should the particle species j have a

gyrotropic VDF, then two of the eigenvalues are equal to each other and to $T_{\perp j}$ and the remaining eigenvalue equals $T_{\parallel j}$. However, this method comes with some limitations. Beyond implicitly relying on gyrotropy, it can amplify the effects of measurement errors, especially at $T_{\perp j} \approx T_{\parallel j}$.

When $T_{\perp j} \approx T_{\parallel j}$, a more reliable method of computing these temperature components is to transform the temperature tensor into a coordinate system aligned with the magnetic field direction, \mathbf{B}_0 .

There are two separate coordinate systems/bases involved in this method. The first is the original coordinate system (GSE), which is defined using the Cartesian unit vectors: \hat{x} , \hat{y} , \hat{z} . The other is the new coordinate system aligned with the magnetic field (MAG), which is represented by the Cartesian unit vectors: \hat{a} , \hat{b} , \hat{c} . Using these definitions, the temperature tensor in the GSE and MAG bases are represented as:

$$\mathbf{T}_j^{(\text{GSE})} = \begin{bmatrix} T_{j,xx} & T_{j,xy} & T_{j,xz} \\ T_{j,yx} & T_{j,yy} & T_{j,yz} \\ T_{j,zx} & T_{j,zy} & T_{j,zz} \end{bmatrix}_{(\text{GSE})}$$

$$\mathbf{T}_j^{(\text{MAG})} = \begin{bmatrix} T_{j,aa} & T_{j,ab} & T_{j,ac} \\ T_{j,ba} & T_{j,bb} & T_{j,bc} \\ T_{j,ca} & T_{j,cb} & T_{j,cc} \end{bmatrix}_{(\text{MAG})} \quad (3)$$

respectively. It is also important to recognize the difference between these two temperature tensors and the temperature tensor \mathbf{T}_j (without a parenthetical superscript) that exists regardless of the coordinate system.

The MAG coordinate system is found using the Gram–Schmidt process detailed in depth in Cheney & Kincaid (2010)—which requires three linearly independent vectors (\mathbf{v}_1 , \mathbf{v}_2 , \mathbf{v}_3). The first vector \mathbf{v}_1 is set in the direction of the background magnetic field, \mathbf{B}_0 . Vectors \mathbf{v}_2 and \mathbf{v}_3 are set as the two eigenvectors of the temperature tensor $\mathbf{T}_j^{(\text{GSE})}$ that are most perpendicular to \mathbf{B}_0 .

The vectors \mathbf{v}_1 , \mathbf{v}_2 , and \mathbf{v}_3 are put through the Gram–Schmidt process, resulting in the three orthonormal vectors that define the MAG coordinate system:

$$\hat{\mathbf{a}}^{(\text{GSE})} = \begin{bmatrix} a_x \\ a_y \\ a_z \end{bmatrix} \quad \hat{\mathbf{b}}^{(\text{GSE})} = \begin{bmatrix} b_x \\ b_y \\ b_z \end{bmatrix} \quad \hat{\mathbf{c}}^{(\text{GSE})} = \begin{bmatrix} c_x \\ c_y \\ c_z \end{bmatrix}. \quad (4)$$

It is imperative that the first vector put through the Gram–Schmidt process is the magnetic field vector, \mathbf{B}_0 . This is to ensure that:

$$\hat{\mathbf{a}} = \hat{\mathbf{B}}_0, \quad \hat{\mathbf{b}} \perp \hat{\mathbf{B}}_0, \quad \hat{\mathbf{c}} \perp \hat{\mathbf{B}}_0 \quad (5)$$

which is important when later calculating ($T_{\perp j}$ and $T_{\parallel j}$) from the rotated temperature tensor $\mathbf{T}_j^{(\text{MAG})}$

The next step in the process is to create a transformation matrix that will rotate a temperature tensor in the GSE coordinate system into the MAG coordinate system. First, take the vectors of the MAG coordinate system to be the columns of the matrix \mathbf{G} :

$$\mathbf{G} = \begin{bmatrix} a_x & b_x & c_x \\ a_y & b_y & c_y \\ a_z & b_z & c_z \end{bmatrix}. \quad (6)$$

Again, it is important to make sure that the vector $\hat{\mathbf{a}}^{(\text{GSE})}$ is in the first column, to ensure that the $T_{\parallel j}$ and $T_{\perp j}$ later calculated from $\mathbf{T}_j^{(\text{MAG})}$ are actually the parallel and perpendicular components, respectively.

\mathbf{G} is the transformation matrix that would rotate a temperature tensor from MAG coordinates into GSE

coordinates. This method requires the opposite, a transformation matrix \mathbf{F} that rotates a temperature tensor from GSE coordinates into MAG coordinates. This is accomplished by taking the inverse of \mathbf{G} , thus:

$$\mathbf{F} = \mathbf{G}^{-1} \quad \text{or} \quad \mathbf{F} = \begin{bmatrix} a_x & b_x & c_x \\ a_y & b_y & c_y \\ a_z & b_z & c_z \end{bmatrix}^{-1}. \quad (7)$$

With \mathbf{F} , the original temperature tensor $\mathbf{T}_j^{(\text{GSE})}$ can be rotated to align with the magnetic field \mathbf{B}_0 :

$$\mathbf{T}_j^{(\text{MAG})} = \mathbf{F}^T \mathbf{T}_j^{(\text{GSE})} \mathbf{F} \quad (8)$$

where \mathbf{F}^T is the transpose of the transformation matrix \mathbf{F} . Written out explicitly, Equation (8) becomes:

$$\begin{bmatrix} T_{j,aa} & T_{j,ab} & T_{j,ac} \\ T_{j,ba} & T_{j,bb} & T_{j,bc} \\ T_{j,ca} & T_{j,cb} & T_{j,cc} \end{bmatrix}_{(\text{MAG})} = \left(\begin{bmatrix} a_x & b_x & c_x \\ a_y & b_y & c_y \\ a_z & b_z & c_z \end{bmatrix}^{-1} \right)^T \begin{bmatrix} T_{j,xx} & T_{j,xy} & T_{j,xz} \\ T_{j,yx} & T_{j,yy} & T_{j,yz} \\ T_{j,zx} & T_{j,zy} & T_{j,zz} \end{bmatrix}_{(\text{GSE})} \begin{bmatrix} a_x & b_x & c_x \\ a_y & b_y & c_y \\ a_z & b_z & c_z \end{bmatrix}. \quad (9)$$

Now the parallel and perpendicular temperatures are found from the diagonal elements of this tensor $\mathbf{T}_j^{(\text{GSE})}$. $T_{\parallel j}$ is simply the first diagonal element while $T_{\perp j}$ is the average of the other two diagonal elements:

$$T_{\parallel j} = T_{j,aa} \quad T_{\perp j} = \frac{T_{j,bb} + T_{j,cc}}{2}. \quad (10)$$

This rotation process was applied to each of the $N = 129,934$ temperature tensors for both protons and alpha particles. The

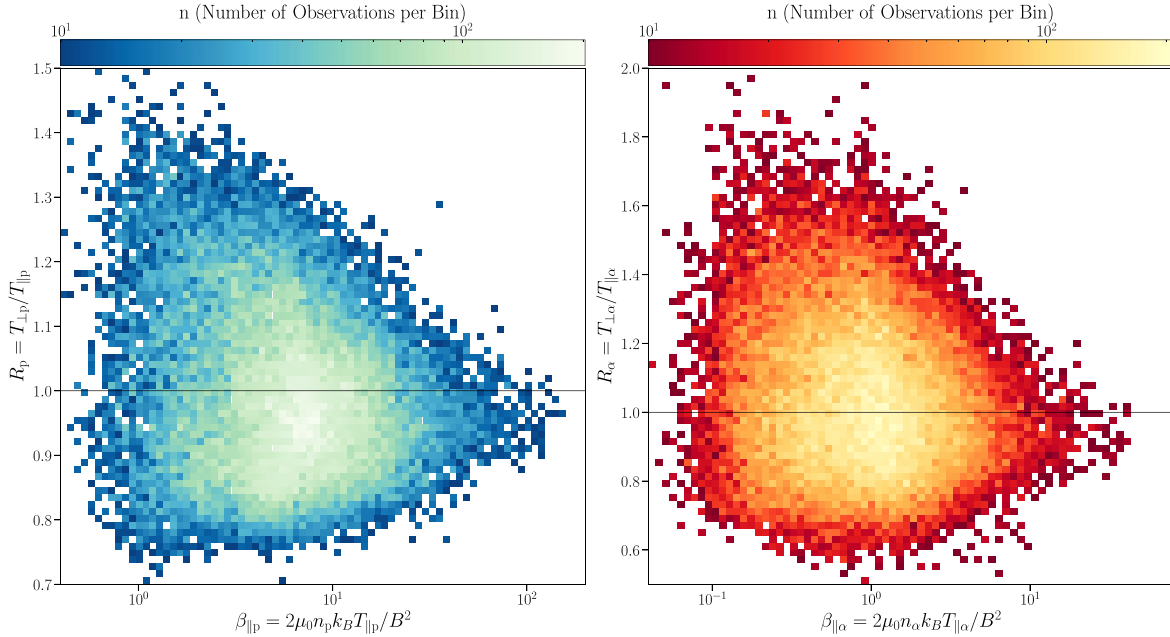


Figure 2. Two plots of the distribution of $(\beta_{\parallel j}, R_j)$ -values of both ions for the MMS data set specified in Table 2. The left-hand plot (blue) is for protons while the right-hand plot (red) is for alpha particles.

bottom row of Figure 1 shows the distributions of these $(T_{\perp j}, T_{\parallel j})$ -values for both protons ($j = p$) and alpha particles ($j = \alpha$). For both particle species, the majority of the plasma is nearly isotropic (i.e., $T_{\perp j} \approx T_{\parallel j}$), which is to be expected in the magnetosheath’s high- $\beta_{\parallel j}$ plasma and is consistent with prior observations by other instruments (Maruca et al. 2018).

4.2. Departures from Gyrotropy and Bi-Maxwellianity

For a truly bi-Maxwellian VDF observed without measurement error, the two perpendicular temperatures, T_{bb} and T_{cc} , would be equal and the off-diagonal elements would be zero. In practice, no plasma VDF is perfectly gyrotropic, and there will always be some measurement error, leading to small variations between T_{bb} and T_{cc} in addition to off-diagonal values that are small (compared to the diagonal elements) but not exactly zero.

Two parameters were introduced to quantify these effects in this study’s data set. First, the departure of a VDF from gyrotropy was quantified by:

$$\delta_{j,\text{gyro}} = \frac{(|T_{j,ab}| + |T_{j,bc}| + |T_{j,ac}|)/3}{(T_{j,aa} + T_{j,bb} + T_{j,cc})/3}. \quad (11)$$

Second, the departure of a VDF from a bi-Maxwellian was quantified by:

$$\delta_{j,\text{bimax}} = \frac{|T_{j,bb} - T_{j,cc}|}{(T_{j,aa} + T_{j,bb} + T_{j,cc})/3}. \quad (12)$$

The median values of these two parameters for protons are $\delta_{p,\text{gyro}} = 5.95\%$ and $\delta_{p,\text{bimax}} = 13.29\%$ and the average values for alpha particles are $\delta_{\alpha,\text{gyro}} = 25.93\%$ and $\delta_{\alpha,\text{bimax}} = 49.11\%$. Two explanations (or a combination thereof) may account for the higher values for the alpha particles versus the protons. First, some studies (e.g., Fuselier et al. 1988) have found that alpha particles exhibit stronger departures from bi-Maxwellianity than protons. Second, alpha particles are far less

abundant than protons and therefore their moments are more subject to measurement error.

4.3. Statistical Analysis

Figure 2 shows distributions of $(\beta_{\parallel j}, R_j)$ -values for both protons (left, blue) and alpha particles (right, red). To generate the proton plot the $(\beta_{\parallel p}, R_p)$ plane was divided into a grid of bins: 75 $\beta_{\parallel p}$ bins (logarithmically spaced from $10^{-0.4}$ to $10^{2.3}$) by 75 R_p bins (linearly spaced from 0.7 to 1.5). To generate the alpha particle plot, the $(\beta_{\parallel \alpha}, R_{\alpha})$ plane was once again divided into a grid of bins: 75 $\beta_{\parallel \alpha}$ bins (logarithmically spaced from $10^{-1.4}$ to $10^{1.9}$) by 75 R_{α} bins (linearly spaced from 0.5 to 2.0). The color of each bin indicates (on a logarithmic scale) n , the number of observations from the data set that it contains.

Figure 3 presents slightly modified versions of the plots in Figure 2 that partially correct for the unequal bin sizes along the horizontal axis. Rather than simply showing the number of observations, n , in each bin, each plot in Figure 3 shows an estimate of the probability density of observing a given set of $(\beta_{\parallel j}, R_j)$ -values. The color of each bin indicates (on a logarithmic scale) the probability density,

$$\tilde{p}(\beta_{\parallel j}, R_j) = \frac{n}{N \Delta \beta_{\parallel j} \Delta R_j} \quad (13)$$

where n is the number of data in the bin, N is the total amount of data in the data set, and $\Delta \beta_{\parallel j}$ and ΔR_j are the width of the bin along each axis. The plots were generated by binning the data set using the same method as in Figure 2. Bins with $n < 10$ were deemed statistically insignificant and ignored.

The overlaid curves in Figure 3 show contours of constant growth rate, γ_{max} , across the $(\beta_{\parallel j}, R_j)$ plane. γ_{max} is the growth rate of the fastest growing mode for the set of $(\beta_{\parallel j}, R_j)$ -values and is normalized to the proton cyclotron frequency,

$$\Omega_p = \frac{q_p B}{m_p} \quad (14)$$

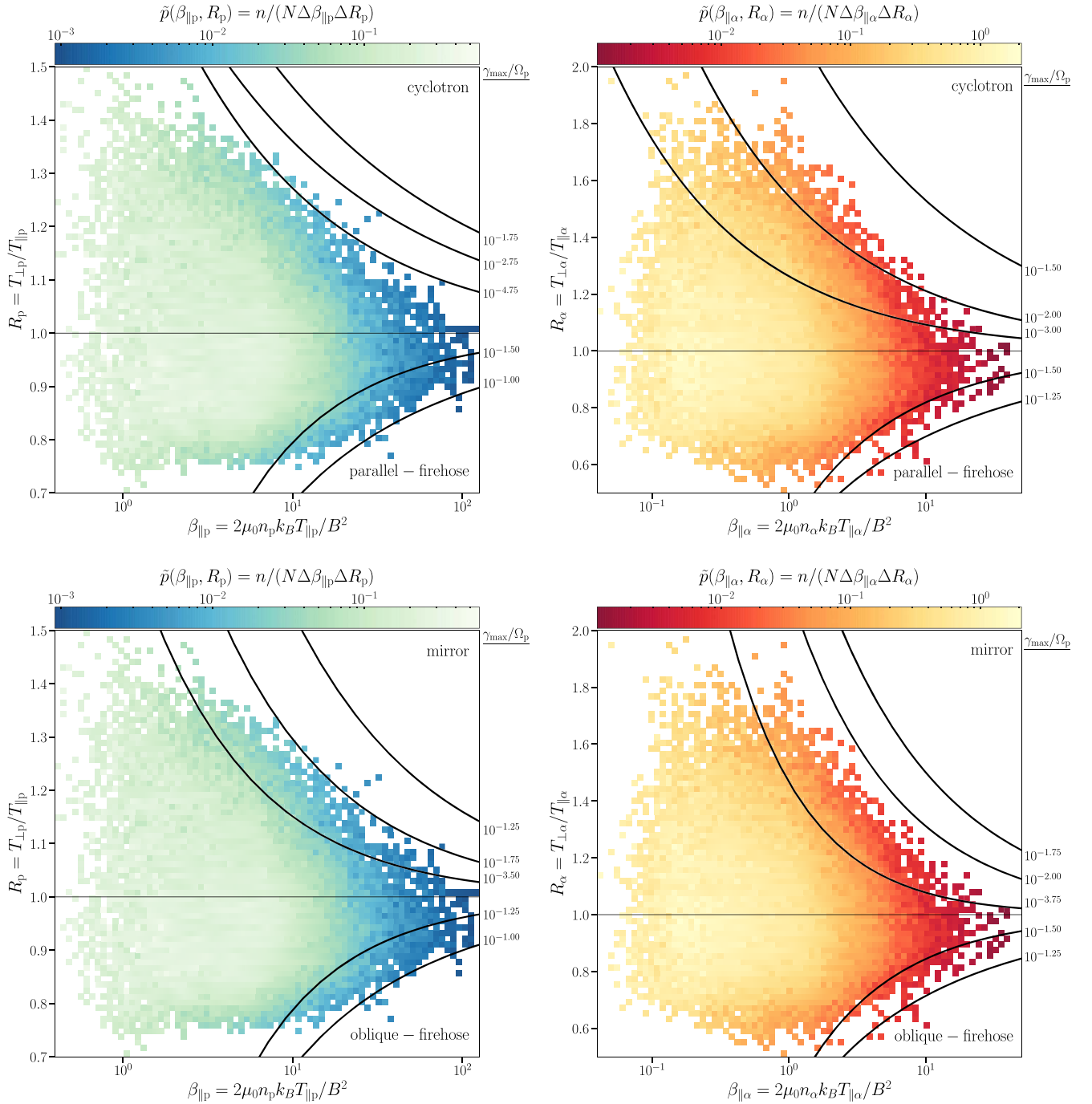


Figure 3. The plot of the probability density, \tilde{p} , of $(\beta_{\parallel j}, R_j)$ -values of both ions for the MMS data set specified in Table 2. The two left-hand plots (blue) are for protons, while the two right-hand plots (red) are for alpha particles. The two plots for each ion are the same, save for the instability contours of constant growth rate overlaid on top of them. The top row of figures depicts the contours for the cyclotron and parallel firehose instabilities and the bottom row depicts the contours of the mirror and oblique firehose instabilities.

where q_p and m_p are the charge and mass of a proton, respectively. The calculations of $\gamma_{\max}(\beta_{\parallel j}, R_j)$ were originally performed by Maruca et al. (2012). For each instability (Table 1) and each ion species ($j=p$ and α), the alpha proton relative abundance was taken to be $n_\alpha/n_p=0.05$ and their relative parallel temperature was taken to be $T_{\parallel\alpha}/T_{\parallel p}=4$. The species were assumed to have no relative drift (i.e., $v_\alpha=v_p$). Based on observations from the Wind spacecraft, Maruca et al. (2012, see Section 3.2) did assume a weak coupling of proton and alpha particle temperature anisotropy. For proton instabilities, the alpha

particle temperature anisotropy was taken to be $R_\alpha = R_p^{0.5}$, and for alpha particle instabilities, the proton temperature anisotropy was taken to be $R_p = R_\alpha^{0.25}$.

Each contour of γ_{\max} in Figure 3 was fit with the analytical model

$$R_j = 1 + \frac{a}{(\beta_{\parallel j} - \beta_0)^b} \quad (15)$$

where a , b , and β_0 are the model's free parameters (Hellinger et al. 2006). For each type of instability, multiple contours of

different growth rates were found using this method. For readability, these contours were split up between two graphs of the same probability distributions, two for protons (left, blue) and two for alpha particles (right, red). The top row of distributions shows the contours for the cyclotron ($R_j > 1$) and parallel firehose ($R_j < 1$) instabilities, while the bottom row shows the contours of the mirror ($R_j > 1$) and oblique firehose ($R_j < 1$) instabilities.

5. Discussion

Figure 3 provides strong evidence suggesting that for both protons and alpha particles, there are $\beta_{\parallel p}$ - and $\beta_{\parallel \alpha}$ -dependent processes working to constrain the temperature anisotropy in the Earth's magnetosheath. In both plots, the range of R_p - and R_α -values gets narrower as $\beta_{\parallel p}$ and $\beta_{\parallel \alpha}$ increase, respectively. These processes also seem to prefer isotropic plasma, as Figure 3 shows that, for any given ($\beta_{\parallel j}$, R_j)-value, the most common R_j -value is one. All of this implies that these processes prefer isotropic ion temperatures and are more active at larger $\beta_{\parallel p}$ and $\beta_{\parallel \alpha}$.

Observations of similar constraints have been found in various space plasma regions, including the solar wind (Matteini et al. 2007; Bale et al. 2009), magnetosheath (Gary et al. 1993; Anderson et al. 1994; Maruca et al. 2018), and the magnetosphere (Anderson et al. 1996). All of these studies have looked at constraints on only proton temperature anisotropies, save for (Gary et al. 1993) which examines constraints on both protons and alpha particle temperature anisotropies in the solar wind.






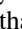


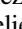

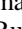
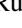

Figure 3 also suggests that kinetic microinstabilities are involved in the processes limiting proton and alpha particle temperature anisotropy in the magnetosheath. The bulk of the data lies within the bounds of the instability thresholds predicted by linear Vlasov theory. Specifically, the contours of the data distribution seem to align with the predicted contours of constant growth rate. This conforms with previous findings demonstrating evidence of instabilities limiting proton temperature anisotropies (Gary et al. 2001; Kasper et al. 2003; Hellinger et al. 2006). There have also been studies examining instability imposed limits on alpha particle temperature anisotropy, such as Maruca et al. (2012) and Bourouaine et al. (2013), but are limited to solar wind plasma only. This study is the first (to the authors' knowledge) to show that this is not a phenomenon exclusive to alpha particles in the solar wind and that the temperature anisotropy of magnetosheath alpha particles is also limited by kinetic microinstabilities.

Prior studies of solar wind protons (Hellinger et al. 2006; Bale et al. 2009) and alpha particles (Maruca et al. 2012) found that the measured probability distribution of ($\beta_{\parallel j}$, R_j)-values aligned better with the growth rate contours of the mirror instability than with those of the ion cyclotron instability, even at $\beta_{\parallel j}$ -value for which the latter instability theoretically set a lower threshold on R_j . In this study, such a clear determination cannot be easily reached as the two instabilities' growth rate contours have relatively similar slopes at magnetosheath's high- $\beta_{\parallel j}$ (see also Maruca et al. 2018).

This study used Level 2 HPCA and FIELDS data products in collaboration with the instrument teams and in accordance with their guidelines. These and all MMS data are available at <https://lasp.colorado.edu/mms/sdc/>. We thank the SDC, HPCA, and FIELDS teams for their assistance with this study.

M.A.S. acknowledges NASA grant 80NSSC20K0198. We would also like to thank the anonymous reviewer of this paper for the extensive and insightful comments.

ORCID iDs

Haley DeWeese  <https://orcid.org/0000-0002-8068-7740>
 Bennett A. Maruca  <https://orcid.org/0000-0002-2229-5618>
 Ramiz A. Qudsi  <https://orcid.org/0000-0001-8358-0482>
 Alexandros Chasapis  <https://orcid.org/0000-0001-8478-5797>
 Elliot Johnson  <https://orcid.org/0000-0002-7326-1864>
 Sarah K. Vines  <https://orcid.org/0000-0002-7515-3285>
 Michael A. Shay  <https://orcid.org/0000-0003-1861-4767>
 William H. Matthaeus  <https://orcid.org/0000-0001-7224-6024>
 Roman G. Gomez  <https://orcid.org/0000-0001-7888-668X>
 Stephen A. Fuselier  <https://orcid.org/0000-0003-4101-7901>
 Barbara L. Giles  <https://orcid.org/0000-0001-8054-825X>
 Daniel J. Gershman  <https://orcid.org/0000-0003-1304-4769>
 Christopher T. Russell  <https://orcid.org/0000-0003-1639-8298>
 Robert J. Strangeway  <https://orcid.org/0000-0001-9839-1828>
 James L. Burch  <https://orcid.org/0000-0003-0452-8403>
 Roy B. Torbert  <https://orcid.org/0000-0001-7188-8690>

References

- Anderson, B. J., Denton, R. E., Ho, G., et al. 1996, *JGR*, **101**, 21527
 Anderson, B. J., Fuselier, S. A., Gary, S. P., & Denton, R. E. 1994, *JGR*, **99**, 5877
 Bale, S. D., Kasper, J. C., Howes, G. G., et al. 2009, *PhRvL*, **103**, 211101
 Bandyopadhyay, R., Begley, L. J., Maruca, B. A., et al. 2022, *GeoRL*, **49**, e2022GL098053
 Bourouaine, S., Verscharen, D., Chandran, B. D. G., Maruca, B. A., & Kasper, J. C. 2013, *ApJL*, **777**, L3
 Burch, J. L., Moore, T. E., Torbert, R. B., & Giles, B. L. 2016, *SSRv*, **199**, 5
 Chen, C. H., Matteini, L., Schekochihin, A. A., et al. 2016, *ApJL*, **825**, L26
 Cheney, W., & Kincaid, D. 2010, *Linear Algebra: Theory and Applications* (Burlington, MA: Jones & Bartlett Learning)
 Fuselier, S. A., Shelley, E. G., & Klumpp, D. M. 1988, *GeoRL*, **15**, 1333
 Gary, S. P. 2005, *Theory of Space Plasma Microinstabilities* (Cambridge: Cambridge Univ. Press)
 Gary, S. P., Anderson, B. J., Denton, R. E., et al. 1993, *GeoRL*, **20**, 1767
 Gary, S. P., Skoug, R. M., Steinberg, J. T., & Smith, C. W. 2001, *GeoRL*, **28**, 2759
 Gary, S. P., Thomsen, M. F., Yin, L., & Winske, D. 1995, *JGR*, **100**, 21961
 Gary, S. P., Wang, J., Winske, D., & Fuselier, S. A. 1997, *JGR*, **102**, 27159
 Gomez, R. 2016, *Magnetospheric Multiscale (MMS) Hot Plasma Composition Analyzer (HPCA) Science Algorithms and User Manual*, Technical Report 10160.13-MMS-HPCA_SCI_ALG_UM, Southwest Research Institute https://lasp.colorado.edu/mms/sdc/public/datasets/hpca/10160.13-MMS-HPCA_SCI_ALG_UM_20160310_0.pdf
 Hellinger, P., Trávníček, P., Kasper, J. C., & Lazarus, A. J. 2006, *GeoRL*, **33**, L09101
 Hsu, O., & McCarthy, J. 2014, *Magnetospheric Multiscale (MMS) Project Alignment and Coordinate System Document*, Technical Report 461-SYS-SPEC-0115, NASA
 Huang, J., Kasper, J. C., Vech, D., et al. 2020, *ApJS*, **246**, 70
 Jansen, H., Xingyu, Z., Yajie, C., et al. 2018, *ApJ*, **856**, 148
 Kasper, J., Lazarus, A., Gary, S., & Szabo, A. 2003, in *AIP Conf. Proc.* 679, *Solar Wind Ten: Proc. of the Tenth Int. Solar Wind Conf.* (Melville, NY: AIP), 538
 Kasper, J. C., Lazarus, A. J., & Gary, S. P. 2002, *GeoRL*, **29**, 20
 Lentz, C., Chasapis, A., Qudsi, R. A., et al. 2021, *JGRA*, **126**, e2021JA029438
 Marsch, E. 2006, *LRSP*, **3**, 1
 Marsch, E., Ao, X.-Z., & Tu, C.-Y. 2004, *JGRA*, **109**, A04102
 Maruca, B. A., Chasapis, A., Gary, S. P., et al. 2018, *ApJ*, **866**, 25
 Maruca, B. A., Kasper, J. C., & Bale, S. D. 2011, *PhRvL*, **107**, 201101
 Maruca, B. A., Kasper, J. C., & Gary, S. P. 2012, *ApJ*, **748**, 137
 Matteini, L., Landi, S., Hellinger, P., et al. 2007, *GeoRL*, **34**, L20105

- Osman, K. T., Matthaeus, W. H., Hnat, B., & Chapman, S. C. 2012, [PhRvL](#), **108**, 261103
- Phan, T.-D., Paschmann, G., Baumjohann, W., Sckopke, N., & Luhr, H. 1994, [JGR](#), **99**, 121
- Russell, C. T., Anderson, B. J., Baumjohann, W., et al. 2016, [SSRv](#), **199**, 189
- Tan, L. C., Fung, S. F., Kessel, R. L., et al. 1998, [GeoRL](#), **25**, 587
- Torbert, R. B., Russell, C. T., Magnes, W., et al. 2016, [SSRv](#), **199**, 105
- Verscharen, D., Klein, K. G., & Maruca, B. A. 2019, [LRSP](#), **16**, 1
- Young, D. T., Burch, J. L., Gomez, R. G., et al. 2016, [SSRv](#), **199**, 407
- Zhang, L., He, J., Zhao, J., Yao, S., & Feng, X. 2018, [ApJ](#), **864**, 35